

5

SIMULATION OF ATOMIC POISEUILLE FLOW UNDER THE INFLUENCE OF THREE-BODY FORCES

In this chapter we explain the general simulation considerations and present our simulation results for atomic fluids. In Chapter 2 we derived the pressure tensor and heat flux vector for inhomogeneous fluids under the influence of three-body forces. In order to validate our derivation, we perform nonequilibrium molecular dynamics simulations of a confined fluid acted upon by a two-body Barker-Fisher-Watts (BFW) force coupled with the Axilrod-Teller (AT) three-body force. Our method of planes calculations agree perfectly with the equivalent mesoscopic route of integrating the momentum and energy continuity equations directly from the simulation data. Our calculations reveal that three-body forces on simple liquids like argon have an important consequence for the isotropic pressure, but have negligible influence on the shear stress and strain rate (hence viscosity) and heat flux vector (hence thermal conductivity). This chapter is based on work published in [44].

5.1 General simulation considerations

The geometry of our simulation cell is shown in Fig. 5.1 and Fig. 5.2. An atomic fluid is confined between atomistic walls as depicted. Our geometry is such that $y = 0$ defines the centre of the fluid channel. A constant field drives the fluid and is directed in the x direction. Each wall is three atomic layers thick, and the second wall is just the periodic image of the first. The entire cell is thus periodic in x , y , and z . The total number

of atoms is $N = 324$, which includes 270 liquid atoms and 54 wall atoms ($N_w = 18$ atoms per layer). In what follows all quantities are expressed in terms of Lennard-Jones reduced units defined in terms of σ , ε and m : reduced distance $r_{ij}^* = r_{ij}/\sigma$, the density $\rho^* = \rho\sigma^3$, the temperature $T^* = k_B T/\varepsilon$, the energy $U^* = U/\varepsilon$, the time $t^* = t/(\sigma\sqrt{m/\varepsilon})$, the pressure $\mathbf{P}^* = \mathbf{P}\sigma^3/\varepsilon$, the strain rate $\dot{\gamma}^* = \sqrt{m\sigma^2/\varepsilon}\dot{\gamma}$, and the viscosity $\eta^* = \sqrt{\sigma^4/(m\varepsilon)}\eta$. For simplicity of notation, hereafter the asterisk will be omitted. We set $\sigma = \varepsilon = m = 1$. The density of the fluid is 0.44 and the wall density is 0.84. The cell dimensions are $L_x = 5.0565$, $L_y = 27.5143$, $L_z = 5.0565$. The thickness of the walls is $\Delta y_w = 2.5143$. The pore width, L , is defined as the distance between the centres-of-mass of the two innermost opposing wall layers. A cutoff potential radius of $L_x/2 = 2.5282$ is used for the two-body force calculation, whereas a value of $L_x/4 = 1.2641$ is used for the three-body force. These are optimal values, based upon the work performed in [56]. In our simulations we use a truncated and shifted version of the BFW and AT potentials, so that long-range corrections need not be considered. In this way the potential is zero at and beyond the cutoff value. We justify this as our goal is to verify the MOP expressions derived in Chapter 2 for the pressure tensor and heat flux vector, rather than to accurately reproduce experimental results.

Our simulations are performed on fluid and solid atoms that interact via the Barker-Fisher-Watts two-body potential [51] and Axilrod-Teller three-body potential [52] introduced in Chapter 3. The equations of motion used to simulate wall and fluid atoms were developed in [45] and quoted here as follows, modified for three-body forces. We note that wall atoms interact via the two plus three body forces in addition to a harmonic spring force that tethers them together. For the wall particles,

$$\dot{\mathbf{r}}_i = \frac{\mathbf{p}_i}{m} \tag{5.1}$$

$$\dot{\mathbf{p}}_i = -\kappa(\mathbf{r}_i - \mathbf{q}_i) + \mathbf{F}_i^{(2)} + \mathbf{F}_i^{(3)} - \alpha\mathbf{p}_i - \mathbf{j}\lambda_{L_n}, \quad i \in L_n \tag{5.2}$$

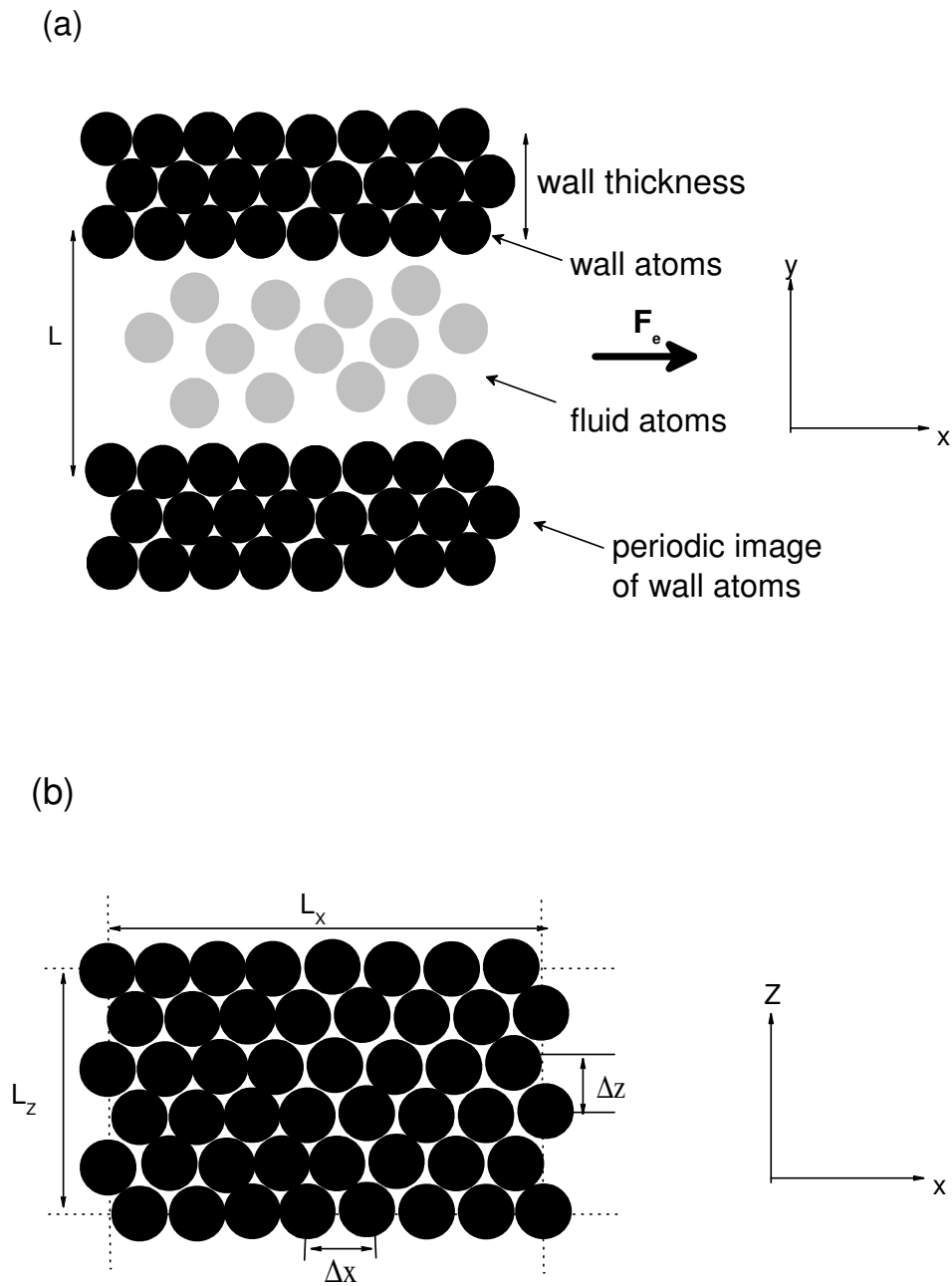


Figure 5.1: Geometry of the simulation environment. (a) Overall system including fluid and wall atoms (z -direction normal to page); (b) wall atoms in the xz plane, defining separation of layers (y -direction normal to page).

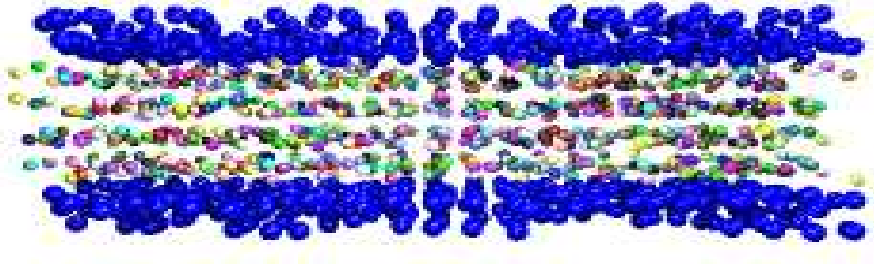


Figure 5.2: Snapshot of the simulation. Black particles represent the walls and the others confined between the black particles are fluid particles.

where κ is the spring force constant and is set to 57.15 in the simulations. \mathbf{q}_i is the equilibrium “frozen” position of atom i . \mathbf{r}_i is the laboratory position of atom i and \mathbf{p}_i here refers to the laboratory momentum of atom i . As the walls are not under the influence of a driving field the peculiar (thermal) and laboratory momenta are equivalent. \mathbf{j} is the unit vector in the y -direction and the layer multiplier λ_{L_n} ensures that the centre of mass of each wall layer stays fixed, where the index $n = 1, 2, 3$, refers to the three wall layers. This is important otherwise the walls separate as the fluid heats up under flow. α is a thermostat multiplier used to keep the temperature of the walls fixed (in our simulations the wall temperature is fixed at 0.722). The layer multiplier and thermostat are computed as

$$\lambda_{L_n} = \frac{\mathbf{j}}{N_w} \sum_{i \in L_n}^{N_w} \left[-\kappa(\mathbf{r}_i - \mathbf{q}_i) + \mathbf{F}_i^{(2)} + \mathbf{F}_i^{(3)} \right] \quad (5.3)$$

where

$$\sum_{L_n=1}^3 \sum_{i \in L_n}^{N_w} 1 = 3N_w$$

and

$$\alpha = \frac{\sum_{i \in L}^{3N_w} \left[-\kappa(\mathbf{r}_i - \mathbf{q}_i) + \mathbf{F}_i^{(2)} + \mathbf{F}_i^{(3)} - \mathbf{j}\lambda_{L_n} \right] \cdot \mathbf{p}_i}{\sum_{i \in L}^{3N_w} \mathbf{p}_i^2} \quad (5.4)$$

Here $L = \{L_1, L_2, L_3\}$ representing the wall layers, and N_w is the number of wall atoms.

The fluid atoms obey Newton's equations of motion

$$\dot{\mathbf{r}}_i = \frac{\mathbf{p}_i}{m} \quad (5.5)$$

$$\dot{\mathbf{p}}_i = \mathbf{F}_i^{(2)} + \mathbf{F}_i^{(3)} + \mathbf{i}F_e \quad (5.6)$$

where F_e is the external driving field and \mathbf{i} is the unit vector in the x -direction and we again note that \mathbf{r}_i and \mathbf{p}_i refer to the laboratory position and momentum of atom i respectively. In our simulations the field strength used is $F_e = 0.2$.

The equations of motion are solved with a fifth order Gear predictor-corrector scheme with an integration time step of $\tau = 0.001$. Our simulations are first run for a total of 10^6 time steps to reach a nonequilibrium steady-state. Once steady-state is achieved, production runs of a total of 10^6 time steps are run with averages accumulated in blocks of 50000 time steps. For clarity of visualisation, we do not put error bars on most of the simulation data throughout this thesis as they are the size of the plotting symbol.

In our simulations we do not assume any functional form for the streaming velocity. Rather, we first run a steady-state simulation of 10^6 time steps and compute a time-averaged velocity profile at planes, using the procedure developed in [62]. These plane velocity values are then used as the streaming velocity $u_x(y)$ in MOP calculations of the pressure tensor and heat flux vector in all subsequent production runs.

Finally, we note that a total of 200 planes are used in the MOP calculations, though not all planes data are plotted on the figures presented in this work for clarity of visualisation. The further details of the simulation methodology can be referred from [45, 46, 62].

5.2 Simulation results

5.2.1 Number density and streaming velocity

Strongly oscillatory surface forces measured with the Surface Forces Apparatus (SFA) were first reported for small molecules confined between atomically smooth mica plates [63].

The existence of such oscillating surface forces suggested that confined fluids are inhomogeneous near the surface. In our simulation, we observe density fluctuations in the vicinity of the solid surfaces, in the form of layers, shown in Fig. 5.3. The layered structure near the solid walls has the same physical origin as the oscillations in the radial distribution function of simple liquids [64, 65]. It can be understood easily for the reference system of a hard sphere fluid next to a hard wall. For this system the inter particle interactions are characterized by the complete absence of any attraction. The actual hard wall - hard sphere potential is infinite when a hard sphere penetrates the wall and zero otherwise. The effective hard wall - hard sphere interaction in the presence of the other hard spheres is different [64]. When a hard sphere is adjacent to the wall then the collisions with other fluid particles from the opposite direction of the wall are much more frequent than from the side of the wall. As a result, the rest of the fluid particles give rise to a net force pushing this particle towards the wall. Therefore the particles touching the surface are attracted to it due to the asymmetry of their collisions with the other fluid particles. This idea was exploited to explain the oscillations of the radial pair correlation function [64]. In Fig. 5.4 we plot the streaming velocity profile. It is seen to be well represented by a symmetric quadratic function in y , when the channel width is more than 10 atomic diameters, in conformity with hydrodynamics [45]. It is well known that hydrodynamics breaks down at smaller channel widths [9].

5.2.2 Pressure tensor

Before we present our simulation results, the methods exploited to compute the pressure tensor and strain rate are briefly outlined.

Elements of the pressure tensor P_{yy} and P_{xy} are computed by the method of planes (MOP). P_{yy} and P_{xy} for the two-body potential are computed by Eqs. (2.36) and (2.45) and those for three-body potential are computed by Eqs. (2.40) and (2.45). All these

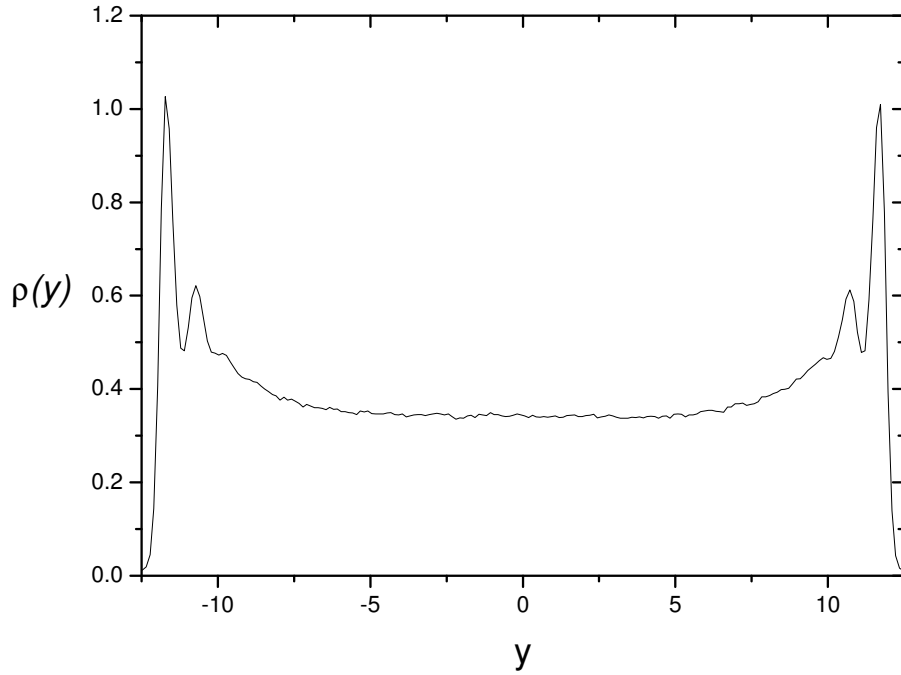


Figure 5.3: Number density profile for the fluid system.

equations were derived in Chapter 2. We compare our method of planes calculations of P_{xy} with the equivalent mesoscopic route of integrating the momentum continuity equation (IMC) [45]. The IMC method is derived as follows. We first write down the momentum continuity equation in the form

$$\rho(\mathbf{r}, t) \frac{d\mathbf{u}(\mathbf{r}, t)}{dt} = -\nabla \cdot \boldsymbol{\Pi} - \nabla p + \rho(\mathbf{r}, t) \mathbf{F}_e \quad (5.7)$$

In this equation $\rho(\mathbf{r}, t)$ is the mass density at position \mathbf{r} and time t , $\mathbf{u}(\mathbf{r}, t)$ the fluid streaming velocity at \mathbf{r} and t , and $\boldsymbol{\Pi}$ the viscous pressure tensor (i.e. $\boldsymbol{\Pi} = \mathbf{P} - p\mathbf{I}$, where \mathbf{P} is the pressure tensor and p the hydrostatic pressure). It is the external force \mathbf{F}_e which drives the flow.

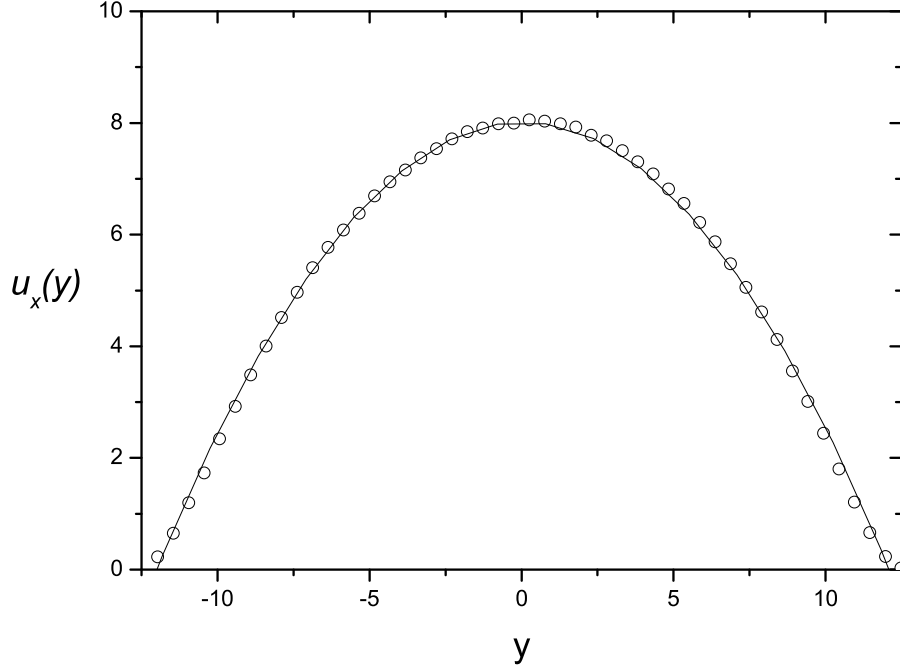


Figure 5.4: Streaming velocity profile (circle data points) for the fluid. Superposed (solid curve) is a symmetric quadratic fit, in conformity with hydrodynamic prediction. Error bars are the size of the plotting symbol.

For our geometry (in the absence of a microscopic pressure gradient), shown in Fig. 5.1, Eq. (5.7) reduces to

$$\frac{\partial \Pi_{xy}}{\partial y} = \rho(y) F_e \quad (5.8)$$

The solution to Eq. (5.8) is

$$\Pi_{xy} = F_e \int_0^y dy' \rho(y') \quad (5.9)$$

In Fig. 5.5 we plot MOP calculations of P_{yy} , the y -component of the pressure in the direction normal to the wall surface, for both the BFW fluid and the BFW fluid with the inclusion of the AT three body forces. For mechanical stability P_{yy} must be constant

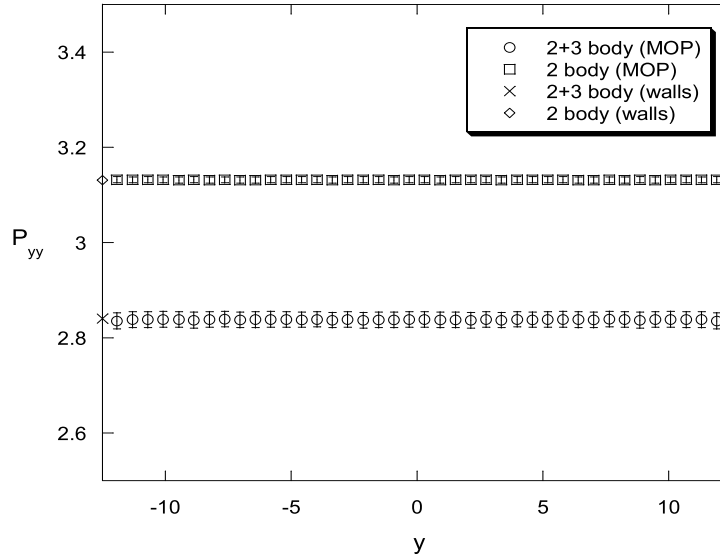


Figure 5.5: P_{yy} as a function of y for the BFW (squares) and BFW+AT (circles) fluids. The pressure is computed by the method of planes. Also shown is the pressure at the walls (crosses for BFW+AT and diamonds for BFW).

throughout the channel, and this is indeed seen to be the case. Also shown is the pressure calculated on the system walls. This is computed from the total y component of the force per unit area exerted on the wall atoms by fluid atoms on one side of the wall. We see perfect agreement between wall and fluid P_{yy} values, as expected. Clearly the addition of the three-body force significantly affects the P_{yy} . Neglecting to include three-body forces overestimates the value by almost 11%.

Of greater interest to us is the shear stress ($-P_{xy}$). In Fig. 5.6 we plot P_{xy} as a function of y for the BFW and BFW+AT fluids. We show the results of our MOP calculations (circle data points for BFW+AT fluids and square for BFW fluids) and compare them with direct integration of the momentum continuity equation, the IMC method given by Eq. (5.9) (solid line for BFW+AT fluids and dash line for BFW fluids). Error bars are of the order of the size of the plotting symbols. We find excellent

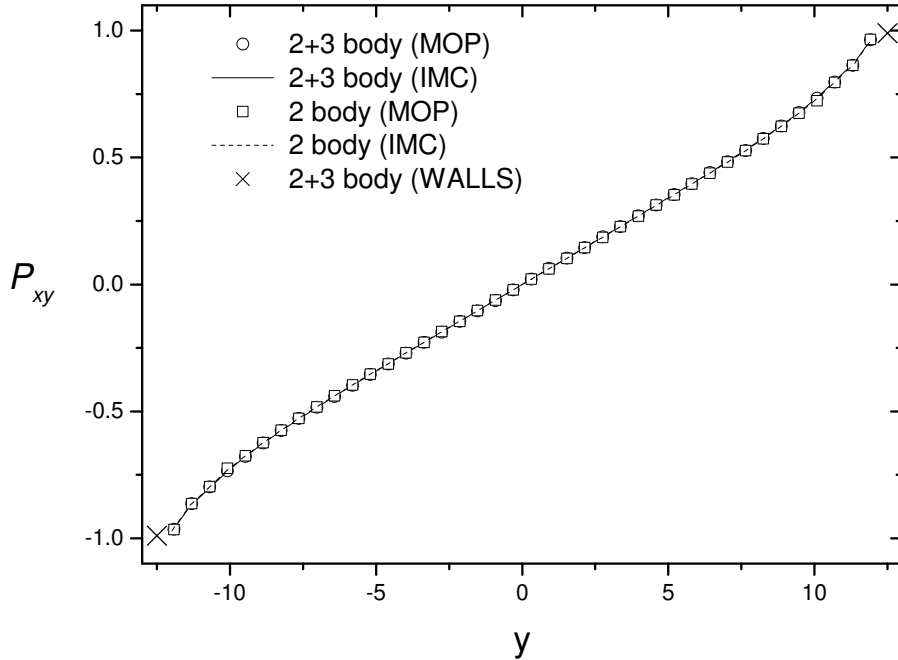


Figure 5.6: P_{xy} as a function of y for the BFW and BFW+AT fluids. P_{xy} computed by the MOP and IMC methods are shown, as well as P_{xy} computed at the walls.

agreement between both methods, demonstrating that the MOP calculations are correct. The value of P_{xy} calculated at the walls (cross data points) is also included and seen to be consistent with both the MOP and IMC values. Note that the stress deviates from the linear hydrodynamics prediction close to the walls, as is to be expected for such a confined system which is inhomogeneous in the vicinity of the walls. From Fig. 5.6 it is clear that three-body forces have negligible effect on the shear stress. This is seen more clearly in Fig. 5.7 in which the region between $5.7 \leq y \leq 6.1$ is magnified. This is consistent with the observations reported in [66] that showed that three-body forces only affected the shear viscosity by approximately 3% for a bulk system under planar Couette flow. The precise degree of influence is likely to depend on temperature and density, and

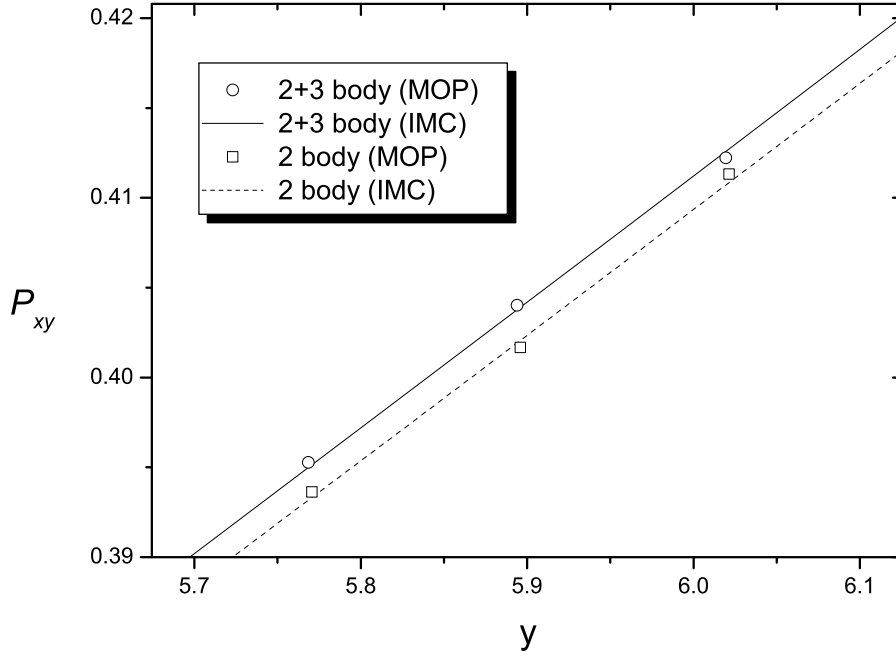


Figure 5.7: As with Fig. 5.6 but magnified in the range between $5.7 \leq y \leq 6.1$.

Error bars are of the order of plotting symbol sizes.

to a lesser degree the number of atoms, so we do not say anything further at this stage. We also note that our potential is truncated and shifted for numerical expediency and this also will affect the longer range attractive contributions to the shear stress.

5.2.3 Heat flux

In Fig. 5.8 we plot the heat flux vector as a function of y for the BFW and BFW+AT fluids. Classical hydrodynamics predicts a cubic heat flux profile. We again show the results of our MOP calculations of J_{Qy} computed by Eqs. (2.59) and (2.60) derived in Chapter 2 and compare them with direct integration of the energy continuity equation,

the IEC method of [46] given as

$$J_{Qy}(y) = - \int_0^y dy' P_{xy}(y') \dot{\gamma}(y'), \quad (5.10)$$

where $\dot{\gamma}(y)$ is the strain rate,

$$\dot{\gamma}(y) = \frac{\partial u_x(y)}{\partial y}. \quad (5.11)$$

Once again, excellent agreement is found between both methods, confirming the validity of the MOP expressions. For a channel this size it is clear that the classical cubic heat flux profile is obeyed. The value of the heat flux at the walls is also computed by noting that the Gaussian thermostat acting on the walls removes heat at a rate of

$$\dot{Q}(t) = \alpha(t) \sum_{i=1}^N \frac{\mathbf{p}_i^2}{m}. \quad (5.12)$$

The heat flux at the walls is therefore

$$\langle J_{Qy}(y = y_{wall}) \rangle = \frac{1}{A} \langle K_w \alpha \rangle, \quad (5.13)$$

where K_w is the kinetic energy of the wall atoms and the angle brackets indicate a time average [46]. The heat flux at the walls is in excellent agreement with the MOP and IEC values at the wall-fluid interface.

We again observe that the presence of three-body forces has very little influence in the transportation of energy across the channel. In Fig. 5.9 the region between $4.0 \leq y \leq 7.0$ is magnified. Three body forces contribute a very small but noticeable effect on the heat flux, slightly increasing its magnitude. Again, this effect is likely to be temperature, density and potential dependent and we refrain from specific conclusions here. What is import for our purposes is the excellent agreement between the MOP and IEC methods.

Finally, in Fig. 5.10 we plot several contributions to the three-body component of the heat flux vector. Term 1 (circles) represents the second and third terms in Eq. (2.58). These terms are the direct three-body analogy of the two-body contribution to the heat

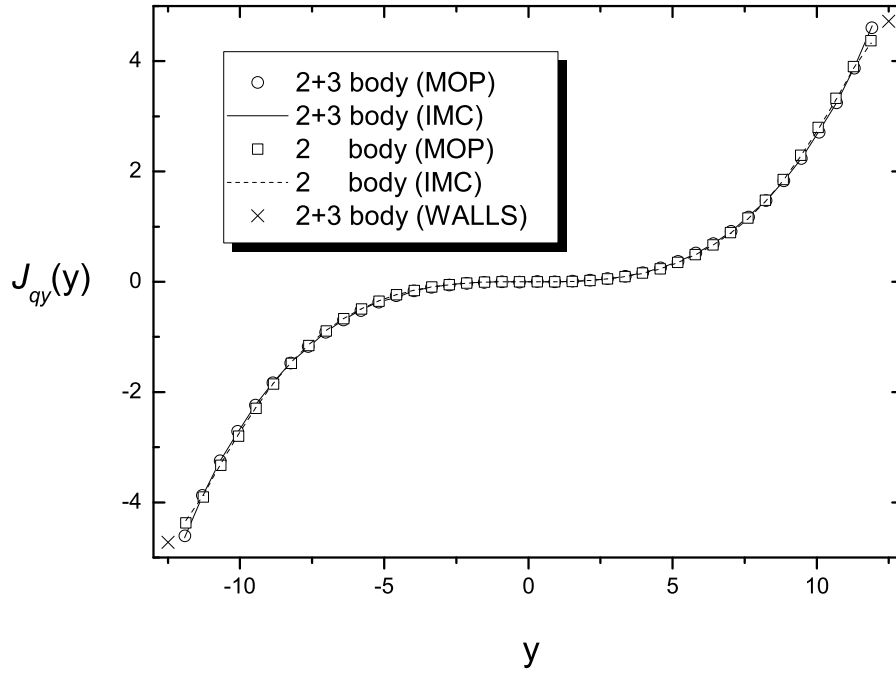


Figure 5.8: Heat flux vector $J_{Qy}(y)$ as a function of y for the BFW and BFW+AT fluids. $J_{Qy}(y)$ computed by the MOP and IEC methods are shown, as well as $J_{Qy}(y)$ computed at the walls.

flux vector. Term 2 (diamonds) represents the additional last three terms in Eq. (2.58). It is clear that these last three terms are negligible, if not zero.

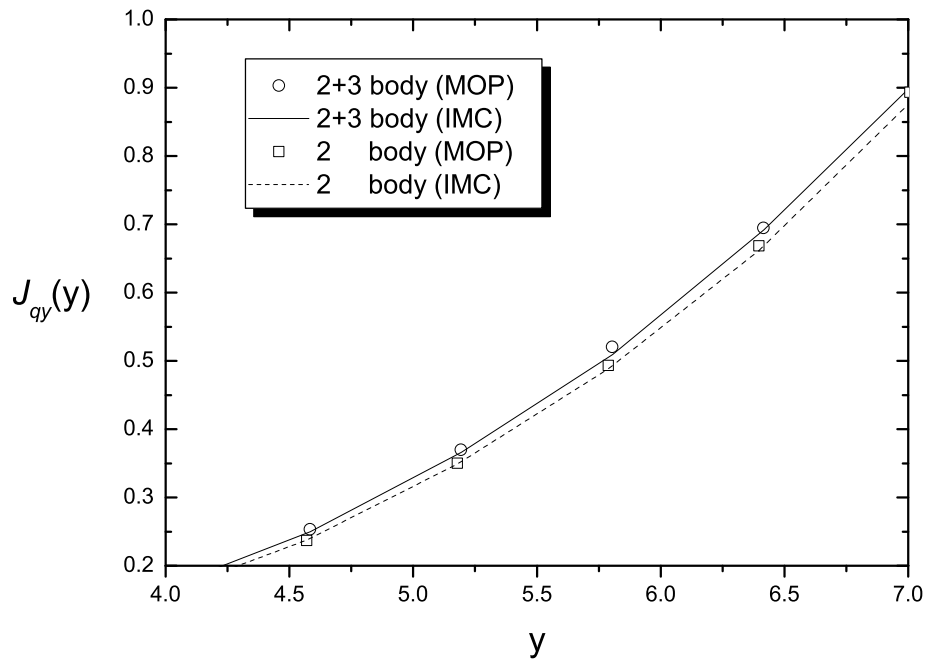


Figure 5.9: As with Fig. 5.8 but magnified in the range between $4.0 \leq y \leq 7.0$.

Error bars are of the order of plotting symbol sizes.

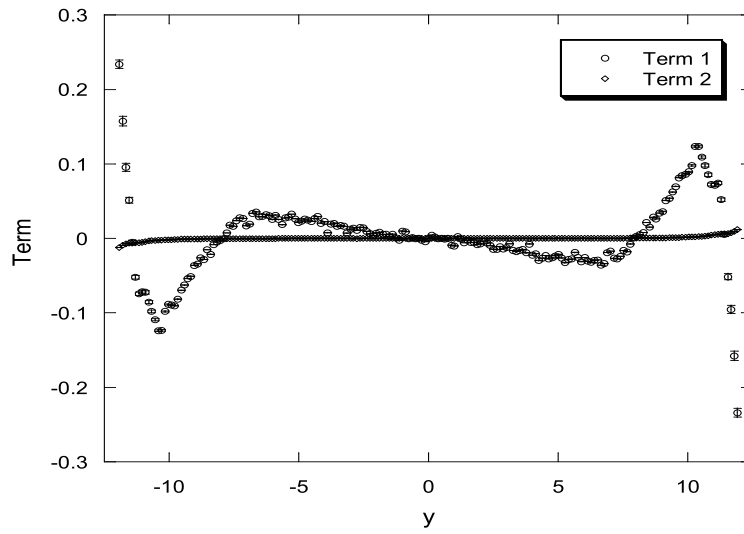


Figure 5.10: Individual terms of the three-body contribution to the heat flux vector.

Term 1 represents the second and third terms of Eq. (2.58) and is the direct analogy of the two-body contribution to the heat flux vector. Term 2 represents the last three terms in Eq. (2.58).